Materials Advances

ROYAL SOCIETY OF CHEMISTRY

PAPER

View Article Online
View Journal | View Issue

Cite this: *Mater. Adv.*, 2021, 2, 3060

Capacity and phase stability of metal-substituted α-$Ni(OH)_2$ nanosheets in aqueous Ni–Zn batteries†

Samuel W. Kimmel,[ab] Brandon J. Hopkins, ‡[b] Christopher N. Chervin,[b] Nathaniel L. Skeele,[b] Jesse S. Ko, §[b] Ryan H. DeBlock, ‡[b] Jeffrey W. Long,[b] Joseph F. Parker,[b] Bethany M. Hudak,[c] Rhonda M. Stroud,[c] Debra R. Rolison *[b] and Christopher P. Rhodes *[a]

Batteries that offer high specific energy and energy density coupled with improved safety and lower cost will affect applications ranging from electric vehicles, portable electronic devices, and grid-level energy storage. Alkaline nickel–zinc (Ni–Zn) batteries use nonflammable aqueous electrolyte and nonstrategic, low-cost electrode materials; however with a two-electron anode, a cathode that stores more than one electron per Ni atom would increase energy density. Herein, we report the effect of substituting metal ions (aluminium, cobalt, manganese, or zinc) into α-$Ni(OH)_2$, a phase that can accommodate more than one-electron charge storage, but which typically converts to lower-capacity β-$Ni(OH)_2$ upon cycling in alkaline electrolytes. We adapt a microwave-assisted process that expresses α-$Ni(OH)_2$ as a high surface-area nanosheet morphology and find that we retain this morphology with all metal-ion substituents. The series is characterized using scanning electron microscopy, transmission electron microscopy, X-ray diffraction, and Raman spectroscopy. Metal-ion substitution influences aggregate growth, interlayer distance, and vibrational frequencies. We test powder-composite cathodes prepared using the substituted α-$Ni(OH)_2$ series *vs.* zinc sponge anodes in alkaline electrolyte under device-relevant mass loadings and using an intentionally aggressive charging protocol to determine onset voltage for oxygen evolution. The electrochemical charge-storage behaviour is established using galvanostatic cycling and differential capacity analysis. The substituents significantly influence both Ni-centred redox and oxygen-evolution voltages (*vs.* Zn/Zn^{2+}). The incorporation of Al^{3+} within α-$Ni(OH)_2$ nanosheets provides higher capacity and phase stability compared to the divalent substituents and unsubstituted α-$Ni(OH)_2$. The presence of ordered free nitrates in the interlayer of Al^{3+}-substituted α-$Ni(OH)_2$, not seen with Co^{2+} or Mn^{2+} substituents, correlates with the improved electrochemical performance.

Received 28th January 2021,
Accepted 25th March 2021

DOI: 10.1039/d1ma00080b

rsc.li/materials-advances

Introduction

Lithium-ion is currently the go-to high-energy battery technology, but its inherent safety issues persist and represent a continued challenge, particularly for large-format applications. To enable wider implementation in electric vehicles and grid-level energy storage, non–lithium-based batteries with high specific energy and energy density, improved safety, and lower cost are essential. The alkaline nickel–zinc (Ni–Zn) battery is an attractive alternative to Li-ion due to its use of nonflammable aqueous electrolyte.

The three-dimensional (3D) aperiodic zinc architecture (“sponge”) developed at the U.S. Naval Research Laboratory solves long-standing performance limitations for zinc anodes[1] and paves the way for next generation Ni–Zn batteries competitive with the specific energy of Li-ion systems.[2] Rewiring the zinc anode as a porous 3D monolith enables more uniform charge and discharge at greater zinc utilization while preventing dendritic growth at the zinc anode. The architected metal opens the door to zinc-based battery chemistries that approach the system-level specific energy and energy density of Li-ion without the accompanying weight and volume of ancillary structures required to mitigate system-failures. A practical Ni–Zn battery provides a specific energy of up to 135 W h kg^{-1} (energy density of ~300 W h L^{-1}) depending on the Zn depth of

[a] *Department of Chemistry and Biochemistry and Materials Science, Engineering and Commercialization Program, Texas State University, San Marcos, TX, 78666, USA. E-mail: cprhodes@txstate.edu*
[b] *U.S. Naval Research Laboratory, Surface Chemistry Branch (Code 6170), Washington, DC, 20375, USA. E-mail: debra.rolison@nrl.navy.mil*
[c] *U.S. Naval Research Laboratory, Materials Science and Technology Division (Code 6300), Washington, DC, 20375, USA*

† Electronic supplementary information (ESI) available: Data and analyses from microscopy, porosimetry, Raman and electrochemistry. See DOI: 10.1039/d1ma00080b

‡ NRL-National Research Council Postdoctoral Associate.

§ Former NRL-National Research Council Postdoctoral Associate.

discharge. The projected specific energy of a fully packaged Ni–Zn system is comparable or superior to a Li-ion pack that includes catastrophe management systems.[2]

Several fabrication iterations of the Zn sponge anode have further improved electrochemical performance, scalability, and mechanical durability such that the capacity of the cathode limits cell performance.[3–8] Deep utilization of the zinc sponge in a Ni–Zn cell for 150 cycles requires swapping out not one, but four commercially harvested nickel hydroxide cathodes per Zn sponge anode.[5,8] Matching the performance of next-generation zinc anodes in terms of capacity and rate requires improving alkaline cathode materials and architectures.

Commercial Ni–Zn batteries use β-$Ni(OH)_2$-based cathodes that have practical capacities of 237–263 mA h g^{-1},[9,10] which capture up to 90% of the theoretical $Ni^{2+/3+}$ one-electron capacity of 289 mA h g^{-1}. Challenges inherent to β-$Ni(OH)_2$ include a steep drop in capacity at high rates and generating γ-NiOOH upon overcharge, which results in large volumetric changes leading to battery failure.[11] Compared to β-$Ni(OH)_2$, α-$Ni(OH)_2$ has a higher theoretical capacity (~487 mA h g^{-1}) storing ~1.67 electrons per Ni center, which partially poises Ni as Ni^{4+} upon charging.[12,13] Electrochemical and spectroscopic support for Ni^{4+} within charged $Ni(OH)_2$ thin films has been previously reported.[14,15] Prior work suggests the oxidation state of Ni is influenced by interlayer ions.[14,16–18] At high pH, α-$Ni(OH)_2$ is unstable converting to β-$Ni(OH)_2$,[19] thus cycling α-$Ni(OH)_2$ in alkaline electrolyte inevitably leads to lower capacity.[20]

Metal substituents can influence the phase stability and electrochemical performance of α-$Ni(OH)_2$. Prior studies find that the stability and charge-storage capacity of α-$Ni(OH)_2$ is affected by such cation substituents as aluminium,[9,21–28] cobalt,[24,25,29–31] copper,[31–34] chromium,[31,35] iron,[31] manganese,[31,35–37] tin,[38] and zinc.[31,39,40] Aluminum (Al) substitution was determined to increase the interlayer spacing and increase discharge capacity relative to unsubstituted α-$Ni(OH)_2$.[9,27,41] Cobalt-substitution into α-$Ni(OH)_2$ accompanied by ethylene glycol intercalation between the layers is reported to stabilize the α-phase when evaluated as an active material in supercapacitors[42] and alkaline batteries.[43] Interlayer distance and electrochemical performance are also affected by anions that accompany the cation substituent.[26]

In addition to the capacity of the cathode, redox potentials are an important consideration when operating within an aqueous alkaline electrolyte because $Ni(OH)_2$ electrocatalyzes the oxygen-evolution reaction (OER). In alkaline electrolyte, OER occurs near the $Ni(OH)_2$/NiOOH redox potential, and as a parasitic reaction, it decreases charge efficiency and lowers discharge capacity.[11] Coprecipitation with a variety of metals can influence the Ni redox potential and either catalyze or poison OER.[31]

The route used to synthesize α-$Ni(OH)_2$ plays a significant role in the resulting morphology, structure, and electrochemical properties.[44] Common routes include chemical precipitation, electrochemical precipitation, sol–gel synthesis, chemical aging, hydrothermal/solvothermal synthesis, and conversion of a nickel alloy.[45] Microwave chemistry provides a rapid synthesis method and can influence the kinetics, selectivity, and yield of chemical reactions.[46] We recently reported that microwave-synthesized α-$Ni(OH)_2$ nanosheets serve as a high surface-area precursor to high-activity bimetallic OER electrocatalysts.[47,48] Microwave synthesis using neutral/mild pH conditions generates α-$Ni(OH)_2$ with a 3D flowerlike morphology[49] unlike the low surface-area aggregates characteristic of highly basic conditions.[44,45,50]

Microwave synthesis has been used to synthesize a number of metal-substituted α-$Ni(OH)_2$ materials such as Mn/Co-substituted α-$Ni(OH)_2$ as a precursor for Ni/Mn/Co oxide materials for supercapacitors,[51] 3D flowerlike Co-substituted α-$Ni(OH)_2$ for supercapacitors,[52,53] and Al/Zn substituted α-$Ni(OH)_2$.[54] These compositions were not explored, however, as active cathode materials in aqueous rechargeable Ni–Zn batteries. We report microwave-synthesized, metal-ion substituted α-$Ni(OH)_2$ and the effects of aluminium, cobalt, manganese, or zinc substitution on morphology, structure and electrochemical performance when formulated into cathodes and cycled *versus* zinc sponge anodes in alkaline Ni–Zn cells. To determine the effect of substituents on oxygen evolution at the Ni cathode, we do not use a charging protocol optimized for coulombic efficiency and long-term cycling; instead, we design an intentionally aggressive one that allows us to evaluate OER onset voltage.

Experimental

Microwave synthesis of $Ni(OH)_2$ nanosheets

The α-$Ni(OH)_2$ nanosheets were synthesized using a microwave-synthesis technique modified from our previously reported microwave-assisted hydrothermal method,[47,48] by adapting the protocol to a large-format microwave reactor at the Naval Research Laboratory (CEM Mars 5 Digestion Microwave System microwave reactor). In the modified synthesis, $Ni(NO_3)_2{\cdot}6H_2O$ (3.0 g, Sigma-Aldrich) and urea (2.46 g, Sigma-Aldrich) were added to a solution of ethylene glycol (63 mL, Sigma-Aldrich) and ultrapure water (9 mL, ≥18 MΩ cm; used for all subsequent reactions). The unstirred solution was exposed to variable microwave radiation at 120 °C for 39 min. The green precipitate was collected by centrifugation and washed five times with water and three times with ethanol (200 proof, Pharmco), and then dried overnight at 60 °C (Fig. 1a).

Metal-substituted α-$Ni(OH)_2$ nanosheets (notated as Ni–M_{10}; M = Al^{3+}, Co^{2+}, Mn^{2+}, or Zn^{2+}) were synthesized by partially substituting M for Ni^{2+} at a Ni-to-M ratio of 9 : 1 (*i.e.*, 10 atomic % substitution). For the metal-substituted α-$Ni(OH)_2$ synthesis, either $Al(NO_3)_3{\cdot}9H_2O$ (0.387 g, Sigma-Aldrich), $Co(NO_3)_2{\cdot}6H_2O$ (0.30 g, Alfa Aesar), or $Zn(NO_3)_2{\cdot}6H_2O$ (0.306 g, Sigma-Aldrich) was added to a solution of $Ni(NO_3)_2{\cdot}6H_2O$ (2.7 g, Sigma-Aldrich), urea (2.46 g, Sigma-Aldrich) ethylene glycol (63 mL, Sigma-Aldrich) and 9 mL of ultrapure water. The respective solutions were then microwaved and washed as described above. The manganese-substituted (Ni–Mn_{10}) reaction was synthesized using a small-scale reactor (CEM Discover SP) at Texas State University, and $Ni(NO_3)_2{\cdot}6H_2O$ (0.9 g, Ward's

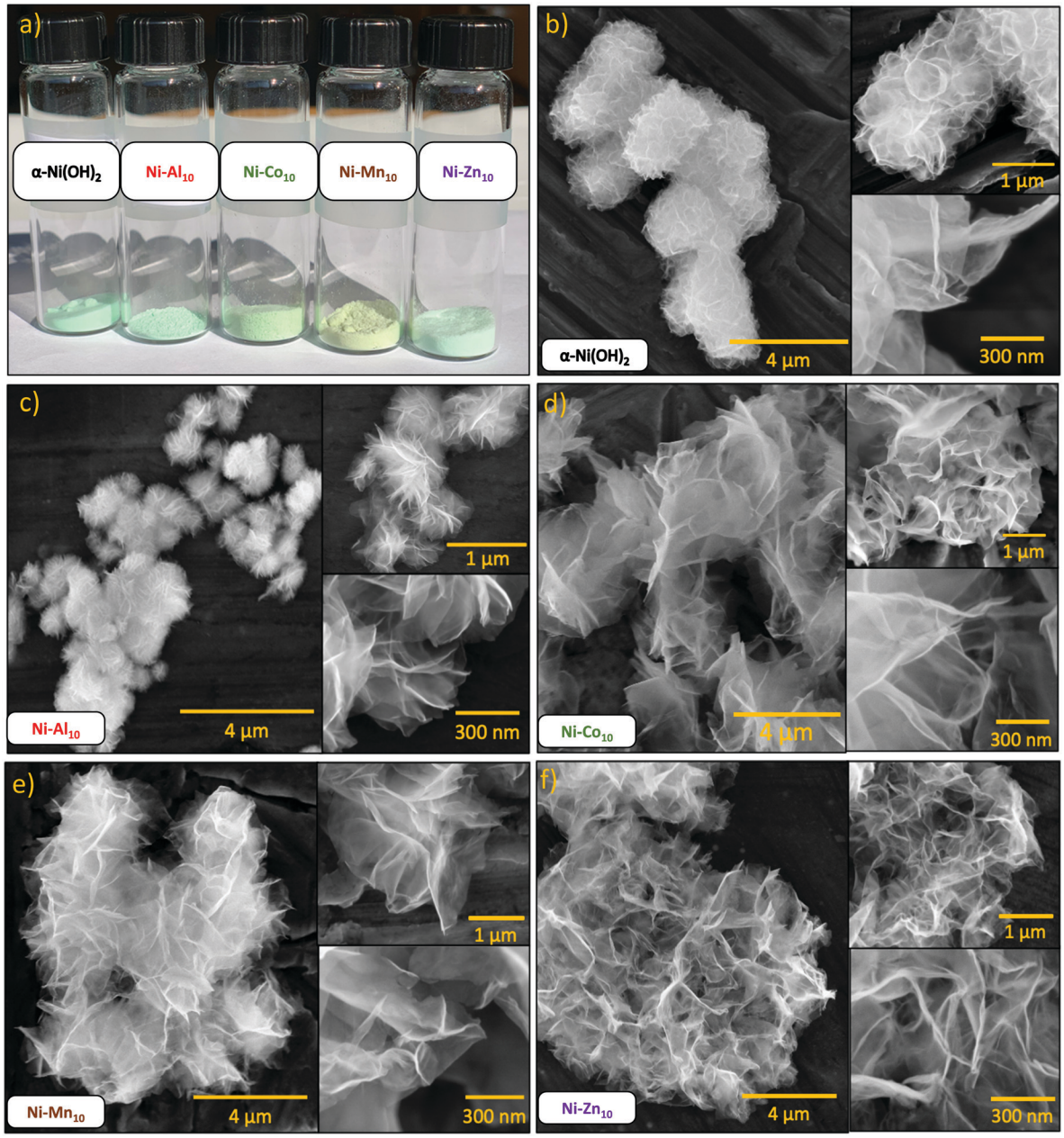

Fig. 1 (a) Photograph of microwave-synthesized powders—25 mg each of unsubstituted α-$Ni(OH)_2$, aluminum-substituted (Ni–Al_{10}), cobalt-substituted (Ni–Co_{10}), manganese-substituted (Ni–Mn_{10}), and zinc-substituted (Ni–Zn_{10}) nanosheets; (b–f) scanning electron micrographs of microwave-synthesized nanosheets at three different magnifications (6500×, 25 000×, 100 000×); (b) unsubstituted α-$Ni(OH)_2$ nanosheets, (c) aluminum-substituted nanosheets (Ni–Al_{10}); (d) cobalt-substituted nanosheets (Ni–Co_{10}); (e) manganese-substituted nanosheets (Ni–Mn_{10}); and (f) zinc-substituted nanosheets (Ni–Zn_{10}).

Science), urea (0.82 g, VWR Analytical) and $Mn(NO_3)_2{\cdot}4H_2O$ (0.086 g, Alfa Aesar) were added to a solution of ethylene glycol (21 mL, VWR Analytical) and ultrapure water (3 mL). The solution was then exposed to variable microwave radiation at 120 °C for 13 min while magnetically stirring. The precipitate was collected and processed as described above (Fig. 1a).

To evaluate potential phase conversions from α-$Ni(OH)_2$ to β-$Ni(OH)_2$, a hydrothermal treatment method was used to treat unsubstituted α-$Ni(OH)_2$ and Ni–Al_{10}. The hydrothermal treatment was adapted from a previously reported method[55] and consisted of placing a suspension of 70 mg of the material and 40.0 mL of 0.01 M NaOH (Alfa Aesar) in a 50 mL Teflon-lined hydrothermal pressure reactor (Parr Instruments Co., model 276AC2) and then heating in a 180 °C-oven for 2 h. The solid was separated by centrifugation and rinsed three times with water and twice with ethanol. The powder was dried overnight at 60 °C.

Materials characterization

Morphology of the microwave-synthesized solids was probed using scanning electron microscopy (SEM; FEI-Helios Nanolab 400).

Nitrogen physisorption measurements were conducted using a Micromeritics ASAP 2020, where the sample was degassed under vacuum at 120 °C for 16 h prior to analysis. Specific surface area was determined by Brunauer–Emmett–Teller (BET) analysis while pore diameters and pore volumes were determined by Barrett–Joyner–Halenda (BJH) analysis of the desorption isotherm. Elemental analysis of the amount of Ni and M within Ni–Al_{10}, Ni–Co_{10}, Ni–Mn_{10}, and Ni–Zn_{10} was determined from inductively coupled plasma-atomic emission spectroscopy (ICP-AES) of digested samples performed by Galbraith Laboratories (Knoxville, TN).

Powder X-ray diffraction measurements (XRD) were performed using a Bruker AXS D8 Advanced powder X-ray diffractometer with a Cu Kα radiation source, operating at 40 kV and 25 mA and a high-resolution energy-dispersive 1D Linxeye XE detector with a 2θ scan range between 5–80° with a 0.01 increment. Raman spectroscopy experiments were carried out using a Horiba LabRam HR evolution confocal Raman spectrometer using a backscattering geometry and a 600 grooves per mm grating. A 514 nm argon-ion laser line focused through a 50×-objective Olympus microscope was used for the excitation source. A laser power of <1 mW at the sample was maintained using a neutral density filter. The Raman instrument was calibrated using the 520.7 cm^{-1} band of Si. The sample was inspected before and after radiation to ensure the sample was not visibly damaged by the incident laser.

Selected samples were imaged by high-angle annular dark-field (HAADF) imaging in a Nion UltraSTEM 200-X scanning transmission electron microscope (STEM) operated at 60 kV with a detector inner semi-angle of 60 mrad. Thickness of the nanosheets was measured using electron energy-loss spectroscopy (EELS) data and calculating the log-ratio absolute thickness using the algorithm in DigitalMicrograph and the following parameters: 10 mrad convergence semi-angle, 50 mrad collection semi-angle, and 24.6 effective atomic number (Z_{eff}).[56] Thickness accuracy is estimated to within 10%.

Electrode and cell fabrication

Ni-foam current collectors (MTI Corp.) were punched out (round, 1/2 inch diameter) and cleaned as recommended by the manufacturer, which consisted of sonicating in an ice bath for 5 min each in concentrated hydrochloric acid (12 M, Fisher Scientific), water, and ethanol (200 proof, Warner-Graham Company). The current collectors were then dried for 10 min under vacuum at 60 °C to remove residual ethanol. Composite cathodes were fabricated by preparing a slurry composed of the active material (α-$Ni(OH)_2$, Ni–Al_{10}, Ni–Co_{10}, Ni–Mn_{10}, or Ni–Zn_{10}), carbon (100% compressed, 99.9%+ acetylene black, Alfa Aesar), and binder (PTFE dispersion in water, Sigma-Aldrich, item number 665800) using a weight percentage ratio of 70 : 25 : 5 for the active material, conductive carbon, and binder, respectively. For preparing the slurry, the active material (60 mg) and conductive carbon (21.4 mg) were mixed by hand with an agate mortar and pestle and then combined with 12–15 drops of water in a vial. The slurry was sonicated for 10 min. The binder was then added, and the mixture was sonicated an additional 10 min. The Ni-foam current collectors were immersed in the slurry and treated under vacuum for 30 min. The cathodes were dried overnight under ambient conditions and then further dried at 60 °C for 2 h. Following drying, the cathodes were pressed by rolling through a pasta roller (Imperia) which produced an electrode 1.26 cm in diameter and 0.4 mm-thick. The average mass loading of active material in the carbon-nanocomposite vacuum-infiltrated Ni-foam electrodes is 11.5 mg cm^{-2}. Achieving >10 mg cm^{-2} represents an important metric to evaluate the performance of $Ni(OH)_2$ electrodes under practical loadings.[57]

Nickel–zinc coin cells were constructed in a similar manner to that previously reported using a ''Gen 3'' zinc sponge as the anode inside a gas-tight laser-cut acrylic alkaline-resistant cell.[5] Briefly, the cells were constructed (from the anode up) using a tin-foil current collector (0.25 mm thick, 99.8% Alfa Aesar), Gen-3 Zn-sponge anode, Celgard separator (3501), Freudenberg separator (700/28), carbon composite cathode embedded in Ni foam, expanded Ni-mesh current collector (Dexmet), and a second Freudenberg separator within gas-tight ethylene propylene diene monomer gaskets. Before cell assembly, the cathode and the separators were vacuum infiltrated with a 6 M KOH/1 M LiOH electrolyte for 30 min (electrolyte volume: 0.3–0.4 mL);[5] the zinc sponge was vacuum infiltrated for the same amount of time in a dispersion of 11 wt% $Ca(OH)_2$ in 6 M KOH/1 M LiOH. The coin-cell experiments were designed such that the capacity of the active cathode material in the cell was significantly lower than the Zn anode capacity enabling a study of the cathode material within a cathode-limited cell configuration. The cells were fabricated in the discharged state using Zn sponge anodes fabricated with ~30 wt% ZnO.[5] Within the cathode-limited cell configuration, the depth of discharge of the Zn anode is $<3\%$.

Electrochemical characterization

Galvanostatic experiments were carried out using an Arbin battery cycler. The cells were charged and discharged at a mass-normalized current rate of 84.4 mA g_{active}^{-1} (0.2C based on a theoretical capacity of 422 mA h g_{active}^{-1} for α-$Ni(OH)_2$) between 1.3 and 2.0 V. During charging, if the cell's theoretical capacity was reached before the upper voltage limit, the cell automatically began discharging. The cycling conditions were not optimized for battery performance but chosen to study the effect that the metal substituents impart on the redox and OER onset voltages of α-$Ni(OH)_2$. We note that the cycling protocol we used to purposefully induce OER will lower coulombic efficiency and contribute to lower electrochemical discharge capacity compared to previous studies.[5,26,34,44]

The cell was charged and discharged four times to activate the cathode material and nickel current collector; these cycles are designated as formation cycles and are not included during cycling analysis.[26,58] The contribution of the Ni-foam current collector to the discharge capacity is negligible ($<1\%$) relative to the active material, in agreement with prior studies.[59,60] The 5th cycle was designated as the starting cycle to evaluate cycling stability. The mass of the active material (α-$Ni(OH)_2$, Ni–Al_{10},

Ni–Co_{10}, Ni–Mn_{10}, or Ni–Zn_{10}) was calculated to be 70% of the weight of the electrode after subtracting the mass of the Ni foam. Reported capacities represent an average obtained from multiple tests. The capacity retention upon cycling was determined by dividing the specific discharge capacity of the 35th cycle by the specific discharge capacity of the 5th cycle.

Differential capacity analysis ($\partial Q/\partial V$) was performed in Origin by taking the derivative of the mass-normalized capacity with respect to the cell voltage. The resulting $\partial Q/\partial V$ plots were smoothed within Origin (FFT Filter) removing all high-frequency signals. The subsequent mass-normalized $\partial Q/\partial V$ plots were fit with Origin's Fit Peak Pro which uses a Levenberg–Marquardt algorithm. Without the use of high-precision $\partial Q/\partial V$ analysis, the raw data required a line smoothing and peak fitting analysis in order to compare samples.[61]

Results and discussion

Analysis of metal-ion substituent composition

During microwave synthesis, selected metal ions (Al^{3+}, Co^{2+}, Mn^{2+}, and Zn^{2+}) are substituted into α-$Ni(OH)_2$ at nominal Ni : M atomic ratios of 9 : 1 (notated as either $Ni_{0.9}M_{0.1}$ or Ni–M_{10}). For comparison to the precursor stoichiometry, the Ni : M ratios measured by ICP are nominal for $Ni_{0.90}Co_{0.10}$, higher than targeted M incorporation for $Ni_{0.87}Al_{0.13}$ and $Ni_{0.84}Zn_{0.16}$, and significantly below target value for $Ni_{0.98}Mn_{0.02}$ (Table 1). Factors that may influence the relative incorporation of metal-ion substituents within the $Ni(OH)_2$ structure include differences in charge density, ionic radii, metal ligand-field strength, solubility product constants, and pH, any of which can influence solution-phase speciation and rates of hydrolysis and condensation.[62] Metal ions with larger ionic radii, such as Zn^{2+} are reported to have higher olation rates while cations with higher ligand-field strength have lower rates of olation due to a greater orbital overlap between metallic d-orbitals and H_2O.[62] Olation rates affect the rate of condensation; rates that are too different between the Ni and the metal substituent may influence the degree of substitution within the $Ni(OH)_2$ structure. Some of these factors likely influence the low relative incorporation of manganese ($Ni_{0.98}Mn_{0.02}$) compared to the targeted synthetic ratio ($Ni_{0.9}Mn_{0.1}$).

Effect of substituents on morphology and porosimetry

Microanalysis of microwave-synthesized α-$Ni(OH)_2$ using high-angle annular dark-field (HAADF) and scanning transmission electron microscopy-energy dispersive spectroscopy (STEM-EDS) confirms a uniform distribution of Ni and O (Fig. S1a and b, ESI†). The material is expressed as stacks of nanosheets with a thickness of ~2 nm (6–7 layers) to ~12 nm (~40 layers) as determined by electron energy-loss spectroscopy (Fig. S2 and Table S1, ESI†). The morphology of α-$Ni(OH)_2$ as evaluated using scanning electron microscopy (SEM) (Fig. 1b) comprises large, round aggregates (diameter ~1.5 μm) of interconnected nanosheet stacks. The lower pH and solution composition of our synthetic protocol, which includes urea and ethylene glycol, leads to wispy, less densely packed layers compared to previously reported nanostructured α-$Ni(OH)_2$.[44,45,50]

Upon partial substitution of Al^{3+}, Co^{2+}, Mn^{2+}, or Zn^{2+} for Ni^{2+}, the overall nanosheet morphology is maintained (Fig. 1c–f); however, the metal-ion substituents influence the size of the aggregated nanosheets. Compared to unsubstituted α-$Ni(OH)_2$, substitution with Al^{3+} affects sheet growth by producing smaller, more densely interwoven nanosheets (Fig. 1c) that aggregate into smaller particulates (~0.5 μm). The remaining substituents result in larger aggregates relative to unsubstituted α-$Ni(OH)_2$: Ni–Co_{10} (~4 μm, Fig. 1d), Ni–Mn_{10} (~3 μm, Fig. 1e) and Ni–Zn_{10} (~10 μm, Fig. 1f). The changes observed in the aggregate size of the microwave-synthesized nanosheets upon substitution may be due to the effects of the metal-ion substituent on solution-phase speciation and hydrolysis and condensation reaction rates, as discussed above.

Nitrogen physisorption analysis tracks the influence of the substituents on BET surface area, average pore diameter, and cumulative pore volume (Table 1). Unsubstituted α-$Ni(OH)_2$ nanosheets exhibit a BET surface area of 87 $m^2\ g^{-1}$, expressing a much higher surface area than materials derived from a microwave-assisted hydrothermal route using water, urea, and $NiCl_2$ (9.2 $m^2\ g^{-1}$).[52] The greatest impact on BET surface area occurs upon substitution with Al^{3+} (40 $m^2\ g^{-1}$), consistent with its more dense aggregates of interconnected nanosheets (Fig. 1c), but which is still higher than NiAl materials synthesized in the presence of EtOH and urea (24.1 $m^2\ g^{-1}$).[63] The surface areas of Ni–Co_{10} (55 $m^2\ g^{-1}$), Ni–Mn_{10} (76 $m^2\ g^{-1}$), and Ni–Zn_{10} (77 $m^2\ g^{-1}$) are lower overall compared to unsubstituted α-$Ni(OH)_2$, but not to the same extent as Ni–Al_{10}.

All substituents decrease the pore volume relative to native α-$Ni(OH)_2$ (Table 1). The pore size distribution plots (Fig. S3, ESI†) indicate that the majority of the free volume for all samples is in the mesopore (>2–50 nm) and macropore range (>50 nm), which is advantageous for electrochemical

Table 1 Physiochemical characteristics of unsubstituted α-$Ni(OH)_2$, aluminum-substituted (Ni–Al_{10}), cobalt-substituted (Ni–Co_{10}), manganese-substituted (Ni–Mn_{10}), and zinc-substituted (Ni–Zn_{10}) nanosheets obtained from elemental analysis (ICP-OES), nitrogen porosimetry, X-ray diffraction, and Raman spectroscopy; details are provided in the text

	Relative atomic % from synthesis	Relative atomic % from ICP analysis	BET surface area ($m^2\ g^{-1}$)	Pore volume ($cm^3\ g^{-1}$)	Interlayer d-spacing (Å)	$\nu(E_g)$	ν(M(O/OH))	ν(–OH stretch)
α-$Ni(OH)_2$	—	—	87	0.579	7.70	458	—	3652
Ni–Al_{10}	$Ni_{0.90}Al_{0.10}$	$Ni_{0.87}Al_{0.13}$	40	0.370	8.72	461	537	3653
Ni–Co_{10}	$Ni_{0.90}Co_{0.10}$	$Ni_{0.90}Co_{0.10}$	55	0.279	8.17	459	521	3656
Ni–Mn_{10}	$Ni_{0.90}Mn_{0.10}$	$Ni_{0.98}Mn_{0.02}$	76	0.380	7.88	447	524	3656
Ni–Zn_{10}	$Ni_{0.90}Zn_{0.10}$	$Ni_{0.84}Zn_{0.16}$	77	0.391	7.81	448	522	3648

applications because this size range improves electrolyte flux to the charge-storing interfaces.[47,64] Substitution with Co^{2+} results in the lowest mesopore volume (Fig. S3, ESI†).

X-ray diffraction

The effects of Al^{3+}, Co^{2+}, Mn^{2+}, or Zn^{2+} substituents on the crystal structure of α-$Ni(OH)_2$ nanosheets are studied by powder X-ray diffraction (Fig. 2). Unsubstituted α-$Ni(OH)_2$ nanosheets exhibit three prominent diffraction peaks at 11.28°, 33.32°, and 59.56° 2θ, which are consistent with the alpha phase of $Ni(OH)_2$ and are assigned as the ⟨001⟩, ⟨110⟩, and ⟨300⟩ planes respectively.[45] The ⟨001⟩ plane corresponds to the reflections of $Ni(OH)_2$ layers within the crystal structure. Prior work on hydrated layered $Ni(OH)_2$ has shown that the position of the ⟨001⟩ peak depends on drying conditions.[65] The broad peak at 23.72° 2θ is assigned as a ⟨002⟩ reflection, which is related to the ⟨001⟩ plane and indicates ordering within the interlayer region. The asymmetric character of the ⟨110⟩ plane is characteristic of the turbostratic disorder of α-$Ni(OH)_2$.[9,26,66]

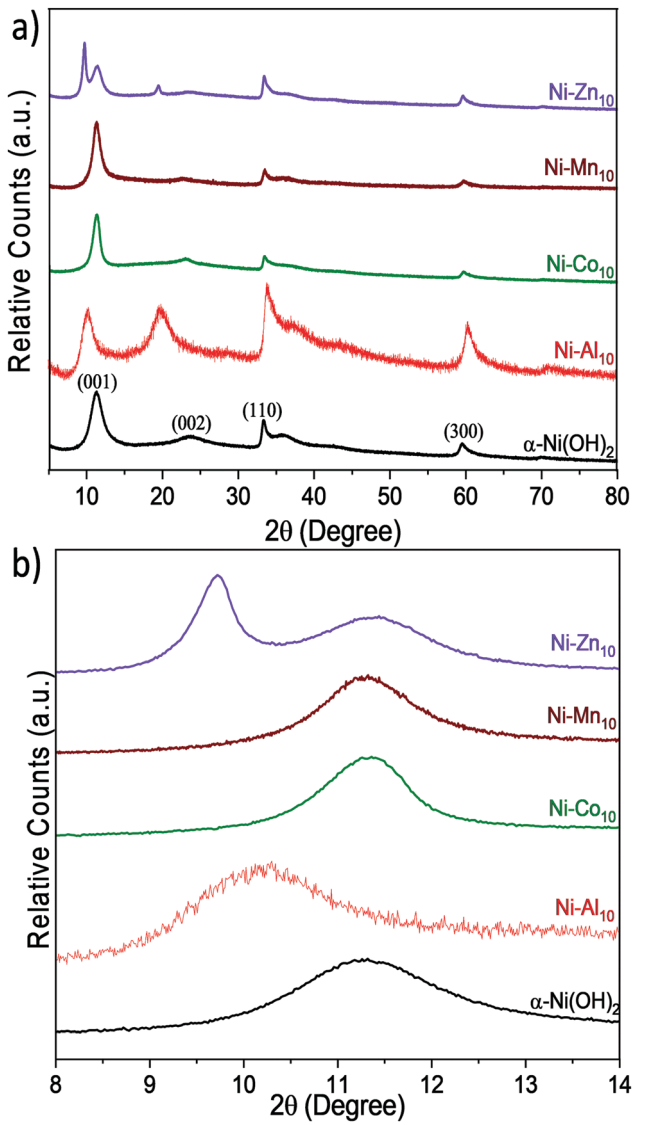

Fig. 2 X-ray diffraction of unsubstituted α-$Ni(OH)_2$, aluminum-substituted ($Ni–Al_{10}$), cobalt-substituted ($Ni–Co_{10}$), manganese-substituted ($Ni–Mn_{10}$), and zinc-substituted ($Ni–Zn_{10}$); (a) diffraction pattern with a 2θ scan range between 5–80°; (b) expanded region for a 2θ scan range between 8–14° showing changes of the ⟨001⟩ plane associated with the interlayer spacing of α-$Ni(OH)_2$.

The effects of substitution on the ⟨001⟩ plane of α-$Ni(OH)_2$ are presented in Fig. 2b and Table 1. The metal substituents shift the ⟨001⟩ peak relative to α-$Ni(OH)_2$; these shifts correspond to larger or smaller interlayer spacings arising from differences in the amounts and coordination of water, anions or other interlayer guests.[26,27,45] In $Ni–Al_{10}$, the interlayer spacing increases from 7.70 Å to 8.72 Å, while STEM-EDS analysis confirms that Al is uniformly distributed within the material (Fig. S1c and d, ESI†). The increased interlayer spacing is attributed to the influx of negatively charged anions such as NO_3^-, OH^-, or CO_3^{2-} required to balance the increased Al^{3+}-derived electrostatic charge.[23,26,27] Within Ni–Al layered hydroxides, anions adopt different orientations and packing within the interlayer.[16,67] A high degree of ordering within the interlayer region of $Ni–Al_{10}$ is evident from the relative intensity of the ⟨002⟩ plane (Fig. 2a). Our Raman data (discussed below) support a higher relative concentration of nitrates within $Ni–Al_{10}$ nanosheets compared to unsubstituted α-$Ni(OH)_2$.

The diffraction pattern of $Ni–Zn_{10}$ shows an additional low-angle peak at 9.72°, not previously observed for Zn^{2+}-substituted α-$Ni(OH)_2$.[39,40,68] The presence of two low-angle peaks within $Ni–Zn_{10}$ is consistent with a two-phase material. Within $Ni–Zn_{10}$, the peak at 11.42° may arise from domains with no or low amounts of Zn^{2+} within the interlayer region, while the peak at 9.72° may result from domains with an interlayer pillared by Zn^{2+}. A prior study of a zinc-containing layered vanadium-oxide material[69] showed that the vanadium oxide layers were pillared by interlayer water and Zn^{2+} ions.

Raman spectroscopy

Raman spectroscopy provides information on the local structure of the substituted α-$Ni(OH)_2$ nanosheets. The substituents shift the frequency of the intralayer $Ni(OH)_2$ asymmetric doubly degenerate E_g lattice mode,[70,71] which indicates that the substituent alters the local potential energy environment (Fig. 3a and Table 1). A previous study of α-$Ni(OH)_2$ correlates frequency shifts in the E_g mode to changes in the Ni–O bond length; shifts to higher wavenumbers indicate a shorter Ni–O bond length, while lower wavenumbers correspond to a longer bond length.[70] Al^{3+}-substitution shifts the E_g mode to a higher frequency suggesting the presence of Al^{3+} shortens the intralayer Ni–O bond length. Co^{2+}-substitution results in a similar $\nu(E_g)$ as α-$Ni(OH)_2$ within experimental error, whereas Mn^{2+} and Zn^{2+} shift the E_g mode to lower frequencies indicating Mn^{2+} and Zn^{2+} increase the intralayer Ni–O bond length. The metal-substituted samples exhibit a new Raman peak between 520 cm^{-1} and 540 cm^{-1}, which may arise from the vibration of a bond of the substituent metal to oxygen/hydroxide $\nu(M(O/OH)_n)$.[72–76] The presence of an additional Raman peak and the absence of an accompanying XRD reflection corresponding to a separate

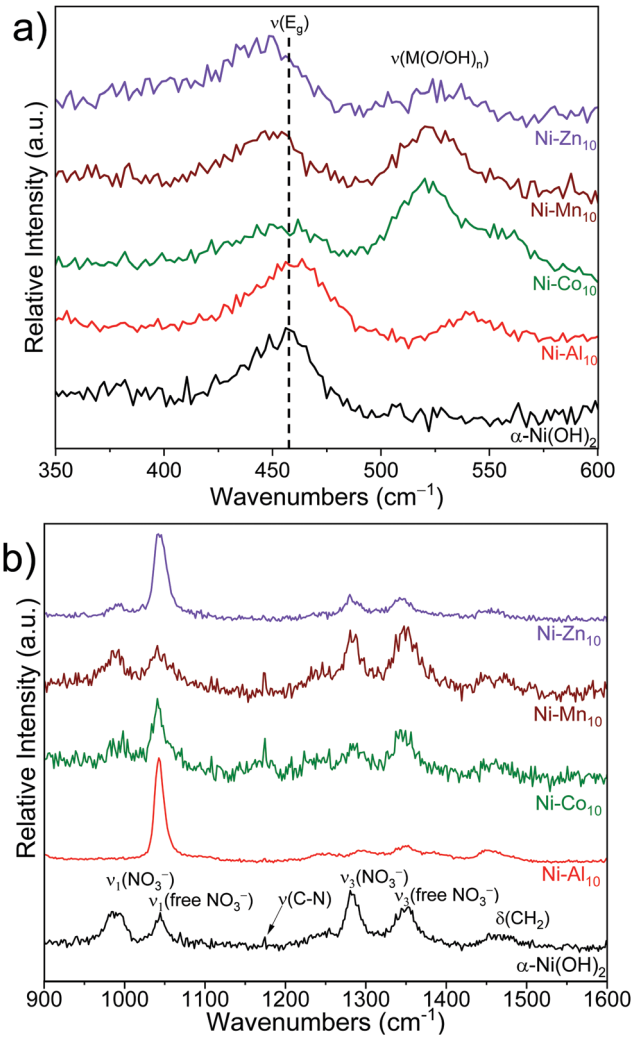

Fig. 3 Raman spectra of unsubstituted α-Ni(OH)$_2$, aluminum-substituted (Ni–Al$_{10}$), cobalt-substituted (Ni–Co$_{10}$), manganese-substituted (Ni–Mn$_{10}$), and zinc-substituted (Ni–Zn$_{10}$): (a) 350 cm^{-1} to 600 cm^{-1} spectral region and assignments of lattice modes; (b) 900 cm^{-1} to 1600 cm^{-1} spectral region and assignments of modes from compounds incorporated into the structure.

phase (with the exception of Ni–Zn$_{10}$) support location of Al^{3+}, Co^{2+}, and Mn^{2+} within the plane of the Ni(OH)$_2$ layer.

Raman-active bands from nitrate anions (NO_3^-) are observed within the unsubstituted α-Ni(OH)$_2$ and metal-substituted α-Ni(OH)$_2$ materials, indicating that nitrates from the synthetic precursors incorporate into the structure. Two distinct nitrate chemical environments are observed (Fig. 3b); one at ~1042 and ~1352 cm^{-1} from a "free" nitrate mode and a second mode at ~986 and ~1283 cm^{-1}.[71] A higher relative intensity of the free NO_3^- peak occurs for Ni–Al$_{10}$ and Ni–Zn$_{10}$ (see also Fig. S4a, ESI†) indicating a higher concentration of nitrates within these samples. Unlike the native and divalent-substituted materials, only free nitrate occurs in Ni–Al$_{10}$. Energetically, nitrate does not associate with Al^{3+} for two reasons: the highly negative free energy of hydration for Al^{3+} compared to first-row transition metals;[62] and compensation of the increased electrostatic charge induced by substitution of Al^{3+} for Ni^{2+}. Based on the increase in the interlayer spacing of Ni–Al$_{10}$ seen by XRD (Fig. 2), these nitrates are located in the interlayer region, consistent with prior studies of layered Ni(OH)$_2$.[42,71]

The frequency of the ν(–OH) stretching mode arising from hydroxides within Ni(OH)$_2$ provides a delineating marker that distinguishes α-Ni(OH)$_2$ from β-Ni(OH)$_2$.[71] The substituted Ni(OH)$_2$ nanosheets exhibit a peak at ~3657 cm^{-1} (Fig. S4b, ESI†) supporting the α-Ni(OH)$_2$ phase assignment made from XRD (Fig. 2). Additional peaks are observed arising from ν(C–H) stretching modes and ν(–OH) bending modes of ethylene glycol,[77] carbonate,[78,79] and cyanate from the decomposition of urea[49,80–83] (Fig. S4, S5 and Table S2, ESI†), which indicate that compounds or derivatives from precursors used in the synthesis are incorporated into the structure.[45]

Electrochemical characterization

Differential capacity analysis of initial charge–discharge. Differential capacity analysis involves taking the derivative of the cell capacity with respect to voltage ($\partial Q/\partial V$) thereby transposing the voltage plateau into well-defined peaks. This method can evaluate gradual changes and failure mechanisms in batteries[58,61,84] and allows for current-controlled measurements that are more translatable to actual devices. In the present work, differential capacity plots are generated directly from the galvanostatic charge–discharge experiments in order to study the influence of substitution on the redox and oxygen evolution voltages of the nickel hydroxide cathodes. The $\partial Q/\partial V$ analysis of unsubstituted α-Ni(OH)$_2$ (Fig. 4 and Table 2) shows an anodic peak centred at 1.80 V assigned to oxidation of $Ni^{2+}(OH)_2$ to $Ni^{3+}OOH$ and a corresponding cathodic peak centred at 1.72 V upon reduction. The anodic current at ~1.94 V corresponds to onset of the parasitic oxygen evolution reaction (OER). Aging studies of α-Ni(OH)$_2$ in H_2O show generation of mixed phase α/β-Ni(OH)$_2$ in as little as four days.[19] Because the formation cycles in this study last from 24–36 h (Fig. S6a, ESI†), unsubstituted α-Ni(OH)$_2$ should already have begun its transformation to β-Ni(OH)$_2$. Unsubstituted α-Ni(OH)$_2$, hydrothermally treated α-Ni(OH)$_2$, and commercial β-Ni(OH)$_2$ have comparable redox peak voltages and discharge capacities (Fig. S7b–d, ESI†), supporting the conclusion that α-Ni(OH)$_2$ nanosheets convert to β-Ni(OH)$_2$ during the formation cycling.

The $\partial Q/\partial V$ analysis of Ni–Al$_{10}$ (Fig. 4) shows that Al^{3+} substitution shifts the anodic and cathodic peaks and OER onset to more positive voltages compared to unsubstituted α-Ni(OH)$_2$ (summarized in Table 2). Because the OER voltage shifts positive, Ni–Al$_{10}$ cathodes offer a wider operational voltage window. The shift in voltage for the Ni-based redox corresponds to a change in chemical potential upon Al^{3+} substitution and is consistent with the frequency shift of the Raman-active E_g lattice mode, as discussed above. Another minor anodic peak appears at a voltage negative of the prominent oxidation peak for Ni–Al$_{10}$ indicating two unique electrochemical environments exist. Possible environments for the minor peak include an Al^{3+}-deficient Ni(OH)$_2$ or a portion of β-Ni(OH)$_2$ within the material.

Ni–Co$_{10}$ cathodes shift the Ni-centred oxidation and reduction peaks and OER onset to lower voltages compared

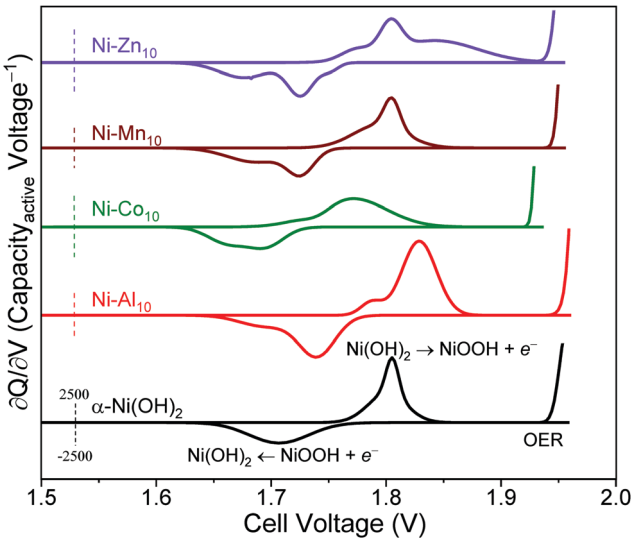

Fig. 4 Mass-normalized differential capacity ($\partial Q/\partial V$) analysis of the 5th cycle galvanostatic charge–discharge of Ni–Zn sponge cells for unsubstituted α-$Ni(OH)_2$, aluminum-substituted (Ni–Al_{10}), cobalt-substituted (Ni–Co_{10}), manganese-substituted (Ni–Mn_{10}), and zinc-substituted (Ni–Zn_{10}) nanosheets at a mass-normalized current of 84.4 mA g_{active}^{-1} between 1.3–2.0 V; height of dashed lines indicates relative intensity of mass-normalized differential capacity.

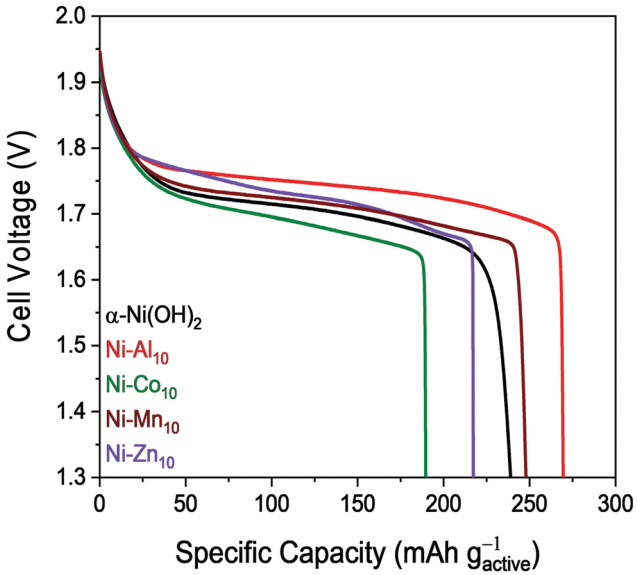

Fig. 5 Voltage *vs.* specific capacity for 5th cycle discharge of Ni–Zn sponge cells for powder-composite cathodes containing unsubstituted α-$Ni(OH)_2$, aluminum-substituted (Ni–Al_{10}), cobalt-substituted (Ni–Co_{10}), manganese-substituted (Ni–Mn_{10}), or zinc-substituted (Ni–Zn_{10}) nanosheets at a mass-normalized current of 84.4 mA g_{active}^{-1} between 1.3–2.0 V.

to unsubstituted $Ni(OH)_2$ (Fig. 4 and Table 2), which is consistent with previous voltammetric studies of Co-substituted α-$Ni(OH)_2$.[30,31,85] Prior work suggests that substitution with Co^{2+} can lower the band gap, increasing the conductivity of $Ni_{0.5}Co_{0.5}$ hydroxide nanosheets relative to α-$Ni(OH)_2$,[86] while another group postulates that $Co(OH)_2$ oxidizes to form a CoOOH network.[52] The anodic and cathodic peak positions and areas of Ni–Mn_{10} (Fig. 4) are similar to that of unsubstituted $Ni(OH)_2$ (Table 2), which is not unexpected given the low relative amount of Mn within the structure ($Ni_{0.98}Mn_{0.02}$). The $\partial Q/\partial V$ plot for Ni–Zn_{10} differs from the other substituents as noted by the emergence of additional anodic and cathodic peaks (Fig. 4), further supporting the existence of a multi-phase material as discussed above.

Galvanostatic discharge voltage profiles and capacities. To evaluate how substitution affects the specific discharge capacity of α-$Ni(OH)_2$ nanosheets, voltage *vs.* specific capacity plots are generated from galvanostatic measurements (Fig. 5); charging profiles are provided in Fig. S6a and b (ESI†). The discharge process of the Ni–Zn battery involves electroreduction of NiOOH in the cathode (eqn (1)), and electrooxidation of the Zn anode (eqn (2)), complexation of divalent Zn with hydroxide ions in the alkaline electrolyte (eqn (3)), and dehydration/precipitation (eqn (4)) reactions at the anode to form ZnO, with an overall net reaction described by eqn (5).[2]

$$2NiOOH_{(s)} + 2H_2O_{(l)} + 2e^- \rightarrow 2Ni(OH)_{2(s)} + 2OH^-_{(aq)} \quad (1)$$

$$Zn_{(s)} \rightarrow Zn^{2+}_{(aq)} + 2e^- \quad (2)$$

$$Zn^{2+}_{(aq)} + 4OH^-_{(aq)} \rightarrow Zn(OH)_4^{2-}{}_{(aq)} \quad (3)$$

$$Zn(OH)_4^{2-}{}_{(aq)} \rightarrow ZnO_{(s)} + H_2O_{(l)} + 2OH^-_{(aq)} \quad (4)$$

$$2NiOOH_{(s)} + H_2O_{(l)} \rightarrow 2Ni(OH)_{2(s)} + ZnO_{(s)} \quad (5)$$

After the initial formation cycling (the first four cycles), all microwave-synthesized samples exhibit a 5th-cycle voltage

Table 2 Electrochemical properties of Ni–Zn sponge cells using unsubstituted α-$Ni(OH)_2$, aluminum-substituted (Ni–Al_{10}), cobalt-substituted (Ni–Co_{10}), manganese-substituted (Ni–Mn_{10}), and zinc-substituted (Ni–Zn_{10}) nanosheet cathodes. Differential capacity analysis of cathodic voltages, anodic voltages, and oxygen evolution reaction (OER) voltages averaged over multiple samples. Average specific discharge capacity for the 5th and 35th cycles determined using galvanostatic analysis at a mass-normalized current of 84.4 mA g_{active}^{-1} between 1.3–2.0 V

	Differential capacity analysis ($\partial Q/\partial V$)			Galvanostatic analysis		
	Cathodic peak voltage (V)	Anodic peak voltage (V)	OER onset voltage (V)	5th cycle (mA h g^{-1})	35th cycle (mA h g^{-1})	Capacity retention[a] (%)
α-$Ni(OH)_2$	1.72	1.80	1.94	249	198	79
Ni-Al_{10}	1.74	1.83	1.96	279	221	79
Ni-Co_{10}	1.69	1.77	1.93	172	137	79
Ni-Mn_{10}	1.72	1.80	1.94	255	192	75
Ni-Zn_{10}	1.73	1.81	1.94	229	167	72

[a] Capacity retention calculated as the ratio of averaged discharge capacity of the 5th and 35th cycles.

plateau between 1.65 V and 1.85 V. The higher discharge voltage for Ni–Al_{10} relative to α-$Ni(OH)_2$ and the other substituted materials (Fig. 5) indicates that Al^{3+} substitution affects the electrochemical potential, an energetics argument that is supported by our Raman analysis. We find that Al^{3+} alters the local chemical environment of Ni charge-storage sites by shortening the intralayer Ni–O bond length. Note that Al^{3+}-substituted α-$Ni(OH)_2$ synthesized under basic conditions, rather than the near pH-neutral conditions of our microwave procedure, also exhibits a higher discharge voltage compared to α-$Ni(OH)_2$.[87]

The voltage–capacity plot of Ni–Al_{10} shows that Al^{3+}-substitution enables a greater discharge capacity of 279 mA h g_{active}^{-1} for the 5th cycle compared to unsubstituted α-$Ni(OH)_2$ nanosheets (Fig. 5 and Table 2). The discharge capacity of 255 mA h g_{active}^{-1} for Ni–Mn_{10} is similar to that of unsubstituted α-$Ni(OH)_2$, but with only 2 at% of Mn present ($Ni_{0.98}Mn_{0.02}$), the similarity to α-$Ni(OH)_2$ is expected. Both Co (172 mA h g_{active}^{-1}) and Zn (229 mA h g_{active}^{-1}) lower the discharge capacity relative to α-$Ni(OH)_2$. Capacity suppression in the presence of Co is attributed in the literature to preventing complete oxidation to γ-NiOOH.[59] The multiphase character of Ni–Zn_{10} complicates comparison to the single-phase materials.

The discharge capacity of our microwave-synthesized α-$Ni(OH)_2$ (249 mA h g_{active}^{-1}) is comparable to the discharge capacity of α-$Ni(OH)_2$ synthesized under basic conditions (269 mA h g_{active}^{-1})[87] and α-$Ni(OH)_2$ synthesized by a sintering process (225 mA h g_{active}^{-1}),[88] but is lower compared to other studies of α-$Ni(OH)_2$.[44,89] The direct comparison with prior studies is complicated by a number of factors that affect capacity including cathode material differences,[44] loading,[57] electrolyte,[90] aging time,[90] and cycling protocols, as well as our deliberately selected non-practical charging parameters resulting in extended oxygen evolution at each charging step (Fig. S6, ESI†). However, the intraseries comparison of the capacities of metal-substituted α-$Ni(OH)_2$ to α-$Ni(OH)_2$ using the same testing conditions supports our conclusion that the substituents influence the discharge capacity.

Analysis of the effect of cycling. The effect of substitution within α-$Ni(OH)_2$ on cycling performance is examined for 35 charge and discharge cycles (Fig. 6a and Table 2). The discharge capacity of unsubstituted α-$Ni(OH)_2$ initially fades within the first ten cycles, stabilizing at ~200 mA h g_{active}^{-1} with modest capacity loss thereafter. Post-formation, Ni–Al_{10} retains a higher capacity over cycles 5–10, whereas the other materials all exhibit a capacity decrease. The whole series stabilizes over cycles 10–35, with Ni–Al_{10} retaining the highest mass-normalized capacity of the series, while Ni–Co_{10} has the lowest capacity. After 35 cycles, the substituted materials show similar capacity retention (72–79%) upon cycling as α-$Ni(OH)_2$ (Table 2).

To evaluate the effect of substitution on cycling, we compared differential capacity plots of the 5th and 35th cycles (Fig. 6b). Upon cycling, the $\partial Q/\partial V$ peaks of unsubstituted α-$Ni(OH)_2$ shift to higher voltages, consistent with transformation to the β-polymorph and in agreement with a previous study reporting β-$Ni(OH)_2$ has a higher oxidation voltage.[11] The metal-substituted samples show

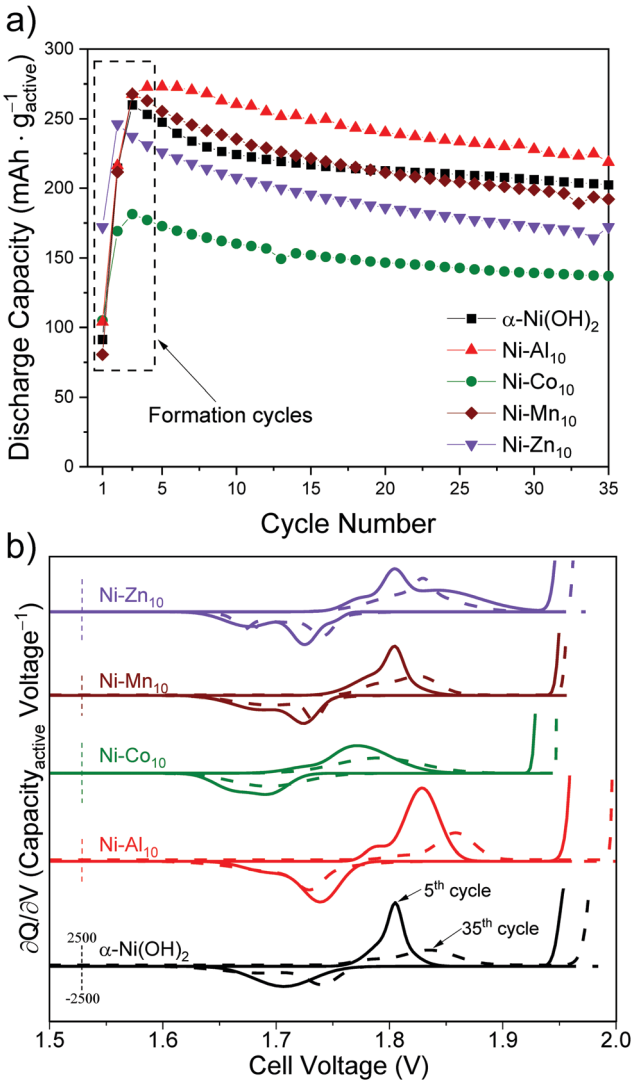

Fig. 6 Analysis of the effect of cycling of Ni–Zn sponge cells for unsubstituted α-$Ni(OH)_2$, aluminum-substituted (Ni–Al_{10}), cobalt-substituted (Ni–Co_{10}), manganese-substituted (Ni–Mn_{10}), and zinc-substituted (Ni–Zn_{10}) nanosheet cathodes at a mass-normalized current of 84.4 mA g_{active}^{-1} between 1.3–2.0 V; (a) specific discharge capacity *vs.* cycle number; (b) comparison of 5th and 35th cycle differential capacity ($\partial Q/\partial V$) *vs.* cell voltage; height of dashed lines in (b) indicates relative intensity of mass-normalized differential capacity; specific discharge capacities reported in (a) were averaged from measurements of multiple samples.

similar shifts of the Ni-centred redox peak to higher voltage (Fig. 6b). In addition to shifting the Ni-centred redox peak positive, the OER onset also shifts to higher voltage. The substituents influence the drift of the OER onset voltage to differing amounts. The shift of the OER onset to higher voltage may result from an increase in internal resistance,[91] differences in the OER active site,[92] or oxygen build up within the electrode[93] as a result of inducing OER because of our intentionally aggressive charging protocol. In particular, the OER voltage shift to more positive values for Ni–Al_{10} provides a wider operational voltage window; the Mn, Co, Zn-substituted materials are subjected to OER for longer duration compared to the Al material (Fig. S6, ESI†). The drift

towards higher voltage will ultimately affect the long-term cycling of the cell. Substituents within α-$Ni(OH)_2$ therefore need to be considered based on their influence on electrochemical charge storage, stability, and effect on redox and OER voltages. The ideal combination is a higher $Ni^{2+/3+}$ redox voltage (to increase the cell voltage *vs.* Zn) while simultaneously shifting OER to a higher voltage. Of the two effects, as desirable is the former, the latter is the more important.

Evaluation of aluminum substitution on stabilization of the α-$Ni(OH)_2$ phase. With the highest capacity of the series, cycling stability, and most positive overvoltage for OER, Al^{3+}-substituted $Ni(OH)_2$ offers promise as an active cathode material over native α-$Ni(OH)_2$. The increased capacity of Ni–Al_{10} occurs despite the 12% lower amount of Ni (41 wt%) compared to α-$Ni(OH)_2$ (48 wt%) indicating that redox-inactive Al^{3+} influences the extent of oxidation of the active Ni sites. The XRD, Raman, and electron microscopic characterization of Ni–Al_{10} provides evidence to support the increased discharge capacity. Of the substituents, Al^{3+} is the only one that creates larger interlayer spacing, a higher concentration of ordered free nitrate between the layers, shorter intralayer Ni–O bond length, and denser packing of nanosheets within the agglomerate. This distinct physical and charge local environment for Ni–Al_{10} correlates with the observed ability to more deeply oxidize the Ni centres.

We note that interlayer free nitrate could play at least two roles: (i) pillar the layers making it energetically unfavourable to collapse the interlayers to form β-$Ni(OH)_2$, and (ii) buffer the electrostatic burden near oxidized Ni sites allowing extra electron charge to be stored and released. Prior studies report that the charge, size, and structure of interlayer anions can influence the oxidation state, discharge capacity, proton transport, and cycle stability of substituted nickel hydroxides.[14,16,26,94,95]

To evaluate whether Al-substitution stabilizes the α-$Ni(OH)_2$ phase, we intentionally treated Ni–Al_{10} and α-$Ni(OH)_2$ at 180 °C for 2 h in 0.01 M NaOH, conditions previously shown to convert α- to β-$Ni(OH)_2$.[55] After hydrothermal treatment, α-$Ni(OH)_2$ retains the nanosheet morphology (Fig. S7a, ESI†). The XRD (Fig. 7a) and Raman (Fig. 7b) data indicate that hydrothermally treated α-$Ni(OH)_2$ (notated as α-$Ni(OH)_2$-AHT) fully converts to the β-phase. In comparison, the XRD pattern of hydrothermal treated Ni–Al_{10} (Ni–Al_{10}-AHT) retains the major peaks associated with the α-phase (Fig. 7a); however, one additional peak at 38.65° 2θ, is consistent with the β-phase. Using the characteristic Raman hydroxyl stretching mode ν(–OH) in $Ni(OH)_2$ to track phase stability, we find that although some β-$Ni(OH)_2$ is present in Ni–Al_{10}-AHT, the α-phase predominates (Fig. 7b). The electrochemical characteristics of α-$Ni(OH)_2$-AHT are similar to α-$Ni(OH)_2$ substantiating that absent Al^{3+} substitution, α-$Ni(OH)_2$ converts to β-$Ni(OH)_2$ during formation cycling (Fig. S7b and c, ESI†).

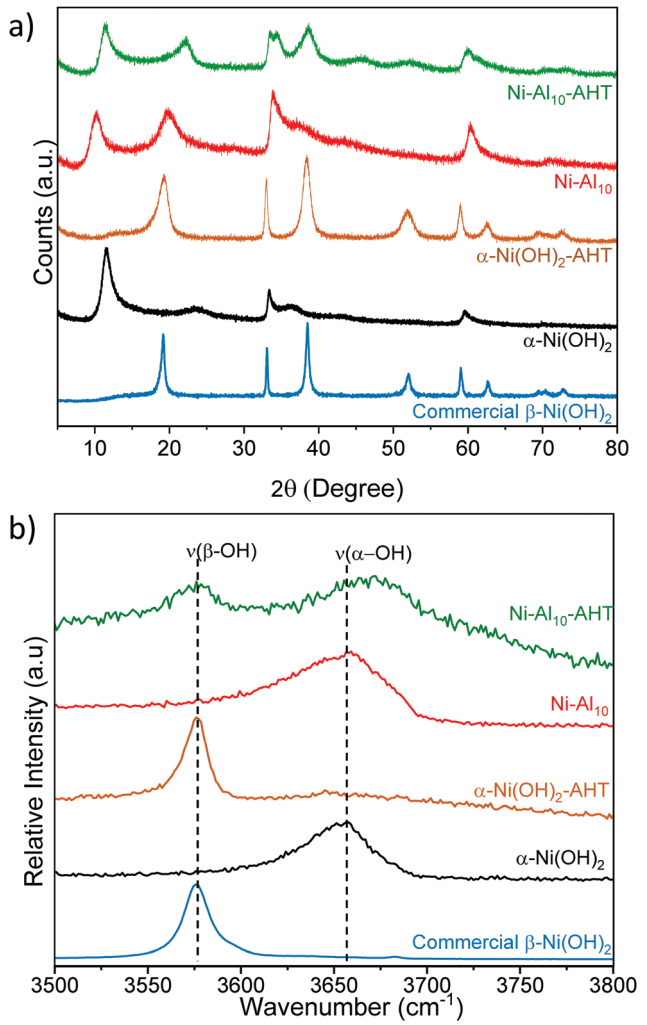

Fig. 7 Effects of hydrothermal treatment on structure of unsubstituted α-$Ni(OH)_2$ and aluminum-substituted (Ni–Al_{10}) nanosheets; (a) X-ray diffraction powder pattern of α-$Ni(OH)_2$, α-$Ni(OH)_2$ after hydrothermal treatment (α-$Ni(OH)_2$-AHT), Ni–Al_{10}, Ni–Al_{10} after hydrothermal treatment (Ni–Al_{10}-AHT), and commercial β-$Ni(OH)_2$ powder (Alfa); (b) Raman spectra in the 3500–3800 cm^{-1} range of α-$Ni(OH)_2$, α-$Ni(OH)_2$-AHT, Ni–Al_{10}, Ni–Al_{10}-AHT, and commercial β-$Ni(OH)_2$ powder.

Conclusions

Metal substituents (Al^{3+}, Co^{2+}, Mn^{2+}, Zn^{2+}) within microwave-synthesized α-$Ni(OH)_2$ nanosheets affect the structure, electrochemical discharge capacity, and phase stability upon electrochemical cycling. Although synthesized to substitute a nominal 10 at%, the metals incorporate within the structure to varying degrees (from 2–16 at%), related to differences in speciation in the reaction medium and rates of hydrolysis and condensation. The native nanosheet morphology is maintained upon substitution. The substituents, however, alter the size of the nanosheet aggregates, surface area, and pore volume.

A layered α-$Ni(OH)_2$ structure is obtained for all substituted materials, and the substituents alter the interlayer distance. Al^{3+} substitution increases the interlayer spacing, consistent with the incorporation of charge-compensating anions within the interlayer. For all substituted α-$Ni(OH)_2$ variants but Zn^{2+}, which results in a two-phase material, the shift in the frequency of the Raman-active E_g lattice mode indicates the substituents change the local potential energy environment of intralayer

Ni–O. Additional Raman peaks support substitution of Al^{3+}, Co^{2+}, and Mn^{2+} within the $Ni(OH)_2$ plane.

The metal-substituted α-$Ni(OH)_2$ cathodes *vs.* Zn-sponge anodes exhibit different behaviour upon galvanostatic charging and discharging. The substituents alter the redox and OER onset voltage, discharge capacity, and capacity retention upon cycling. In this series, Al^{3+} substitution shifts OER onset to the most positive voltage, thereby minimizing parasitic capacity losses. Cathodes prepared with Al^{3+}-substituted α-$Ni(OH)_2$ nanosheets deliver a higher discharge capacity compared to divalent cation-substituted materials, and the higher capacity is retained upon cycling. In agreement with prior work, Al-substitution ensures retention of the α-phase after forced conversion treatment.

From this study we find that the nature of the interlayer plays an important role in the higher discharge capacity of Al^{3+}-substituted α-$Ni(OH)_2$. Different from the other substituents, Al substitution is accompanied by ordered free nitrate anions within the interlayer. The interlayer anions necessary to charge balance a trivalent substituent for divalent Ni stabilize the α-phase by preventing collapse of the layers and by lowering the electrostatic burden at the Ni sites. Both effects enable extra electron charge to be stored and released.

The combination of a nanosheet morphology and Al^{3+} substitution facilitates the development of higher capacity α-$Ni(OH)_2$ cathode materials. To realize energy dense, safe, rechargeable Ni–Zn batteries, we plan to improve cathode performance by exploring different concentrations of Al, the addition of a second substituent, the nature of the interlayer anions, deliberate pillaring of the layers, rethinking the electronic wiring within the cathode structure, and then understanding the effects of these variations on capacity, efficiency, and cycling stability.

Author contributions

C. P. R. and D. R. R. conceived the idea and designed the experiments. C. P. R., D. R. R., C. N. C., J. F. P., and J. W. L. directed the project. S. W. K. prepared the $Ni(OH)_2$ series using microwave synthesis and adapted the synthetic protocol to scale-up quantities of product as advised by D. R. R. N. L. S. replicated selected microwave syntheses. J. S. K., R. H. D., and S. W. K. developed the protocol used by S. W. K. to prepare powder-composite cathodes. B. J. H. fabricated the zinc sponges and designed and laser-cut the coin cells. R. H. D. developed the protocol for differential capacitance measurements. S. W. K. carried out all porosimetry, electrochemical, cycling, and Raman experiments. C. N. C. and S. W. K. performed the X-ray diffraction analyses. S. W. K. performed the scanning electron microscopy and energy-dispersive spectroscopy analyses. B. M. H. performed the transmission electron microscopy measurements and B. M. H. and R. M. S. interpreted the resulting data. S. W. K., C. P. R., and D. R. R. co-wrote the paper. All authors discussed the results, revised, and commented on the manuscript.

Conflicts of interest

There are no conflicts to declare.

Acknowledgements

This work was supported by the Office of Naval Research (ONR). S. W. K., D. R. R., and C. P. R. gratefully acknowledge additional support from the ONR Navy Undersea Research Program Grant No. N00014-19-1-2526 and Naval Research Enterprise Internship Program. J. S. K., B. J. H., and R. H. D. were NRL – National Research Council Postdoctoral Associates.

Notes and references

1 J. F. Parker, C. N. Chervin, E. S. Nelson, D. R. Rolison and J. W. Long, Wiring Zinc in Three Dimensions Re-Writes Battery Performance—Dendrite-Free Cycling, *Energy Environ. Sci.*, 2014, **7**, 1117–1124.

2 J. F. Parker, C. N. Chervin, I. R. Pala, M. Machler, M. F. Burz, J. W. Long and D. R. Rolison, Rechargeable Nickel–3D Zinc Batteries: An Energy-Dense, Safer Alternative to Lithium-Ion, *Science*, 2017, **356**, 415–418.

3 J. F. Parker, E. S. Nelson, M. D. Wattendorf, C. N. Chervin, J. W. Long and D. R. Rolison, Retaining the 3D Framework of Zinc Sponge Anodes upon Deep Discharge in Zn–Air Cells, *ACS Appl. Mater. Interfaces*, 2014, **6**, 19471–19476.

4 J. S. Ko, A. B. Geltmacher, B. J. Hopkins, D. R. Rolison, J. W. Long and J. F. Parker, Robust 3D Zn Sponges Enable High-Power, Energy-Dense Alkaline Batteries, *ACS Appl. Energy Mater.*, 2018, **2**, 212–216.

5 B. J. Hopkins, M. B. Sassin, C. N. Chervin, P. A. DeSario, J. F. Parker, J. W. Long and D. R. Rolison, Fabricating Architected Zinc Electrodes with Unprecedented Volumetric Capacity in Rechargeable Alkaline Cells, *Energy Storage Mater.*, 2020, **27**, 370–376.

6 B. J. Hopkins, C. N. Chervin, M. B. Sassin, J. W. Long, D. R. Rolison and J. F. Parker, Low-Cost Green Synthesis of Zinc Sponge for Rechargeable, Sustainable Batteries, *Sustainable Energy Fuels*, 2020, **4**, 3363–3369.

7 J. F. Parker, I. R. Pala, C. N. Chervin, J. W. Long and D. R. Rolison, Minimizing Shape Change at Zn Sponge Anodes in Rechargeable Ni–Zn Cells: Impact of Electrolyte Formulation, *J. Electrochem. Soc.*, 2015, **163**, A351–A355.

8 B. J. Hopkins, M. B. Sassin, J. F. Parker, J. W. Long and D. R. Rolison, Zinc-Sponge Battery Electrodes that Suppress Dendrites, *J. Visualized Exp.*, 2020, **163**, E61770.

9 J. Li, E. Shangguan, D. Guo, M. Tian, Y. Wang, Q. Li, Z. Chang, X.-Z. Yuan and H. Wang, Synthesis, Characterization and Electrochemical Performance of High-Density Aluminum Substituted α-Nickel Hydroxide Cathode Material for Nickel-Based Rechargeable Batteries, *J. Power Sources*, 2014, **270**, 121–130.

10 M. Urso, G. Torrisi, S. Boninelli, C. Bongiorno, F. Priolo and S. Mirabella, $Ni(OH)_2$@Ni Core-Shell Nanochains as

Low-Cost High-Rate Performance Electrode for Energy Storage Applications, *Sci. Rep.*, 2019, **9**, 7736–7747.
11 Y. Miao, L. Ouyang, S. Zhou, L. Xu, Z. Yang, M. Xiao and R. Ouyang, Electrocatalysis and Electroanalysis of Nickel, its Oxides, Hydroxides and Oxyhydroxides Toward Small Molecules, *Biosens. Bioelectron.*, 2014, **53**, 428–439.
12 V. H. Bode, K. Dehmelt and J. Witte, Uber die Oxydationsprodukte von Nickel(II)-hydroxiden, *Z. Anorg. Allg. Chem.*, 1969, **366**, 1–21.
13 Y. J. Nie, H. X. Yang, J. Q. Pan, W. Li, Y. Z. Sun and H. X. Niu, Synthesis of Nano-Ni$(OH)_2$/Porous Carbon Composite as Superior Cathode Materials for Alkaline Power Batteries, *Electrochim. Acta*, 2017, **252**, 558–567.
14 D. A. Corrigan and S. L. Knight, Electrochemical and Spectroscopic Evidence on the Participation of Quadrivalent Nickel in the Nickel Hydroxide Redox Reaction, *J. Electrochem. Soc.*, 1989, **136**, 613–619.
15 W. E. O'Grady, K. I. Pandya, K. E. Swider and D. A. Corrigan, *In Situ* X-Ray Absorption Near-Edge Structure Evidence for Quadrivalent Nickel in Nickel Battery Electrodes, *J. Electrochem. Soc.*, 1996, **143**, 1613–1616.
16 L. Lei, M. Hu, X. Gao and Y. Sun, The Effect of the Interlayer Anions on the Electrochemical Performance of Layered Double Hydroxide Electrode Materials, *Electrochim. Acta*, 2008, **54**, 671–676.
17 C. Delmas, J. J. Braconnier, Y. Borthomieu and P. Hagenmuller, New Families of Cobalt Substituted Nickel Oxyhydroxides and Hydroxides Obtained by Soft Chemistry, *Mater. Res. Bull.*, 1987, **22**, 741–751.
18 C. Delmas, J. J. Braconnier, Y. Borthomieu and M. Figlarz, From Sodium Nickelate to Nickel Hydroxide, *Solid State Ionics*, 1988, **28–30**(part 2), 1132–1137.
19 D. S. Hall, D. J. Lockwood, S. Poirier, C. Bock and B. R. MacDougall, Applications of in Situ Raman Spectroscopy for Identifying Nickel Hydroxide Materials and Surface Layers During Chemical Aging, *ACS Appl. Mater. Interfaces*, 2014, **6**, 3141–3149.
20 B. Ash, J. Kheti, K. Sanjay, T. Subbaiah, S. Anand and R. K. Paramguru, Physico-Chemical and Electro-Chemical Properties of Nickel Hydroxide Precipitated in the Presence of Metal Additives, *Hydrometallurgy*, 2006, **84**, 250–255.
21 J. Yao, Y. Li, Y. Li, Y. Zhu and H. Wang, Enhanced Cycling Performance of Al-Substituted α-Nickel Hydroxide by Coating with β-Nickel Hydroxide, *J. Power Sources*, 2013, **224**, 236–240.
22 Y. L. Zhao, J. M. Wang, H. Chen, T. Pan, J. Q. Zhang and C. N. Cao, Al-Substituted α-Nickel Hydroxide Prepared by Homogeneous Precipitation Method with Urea, *Int. J. Hydrogen Energy*, 2004, **29**, 889–896.
23 L. J. Yang, X. P. Gao, Q. D. Wu, H. Y. Zhu and G. L. Pan, Phase Distribution and Electrochemical Properties of Al-Substituted Nickel Hydroxides, *J. Phys. Chem. C*, 2007, **111**, 4614–4619.
24 Y. L. Zhao, J. M. Wang, H. Chen, T. Pan, J. Q. Zhang and C. N. Cao, Different Additives-Substituted α-Nickel Hydroxide Prepared by Urea Decomposition, *Electrochim. Acta*, 2004, **50**, 91–98.
25 B. Mavis and M. Akinc, Three-Component Layer Double Hydroxides by Urea Precipitation: Structural Stability and Electrochemistry, *J. Power Sources*, 2004, **134**, 308–317.
26 Y. W. Li, J. H. Yao, C. J. Liu, W. M. Zhao, W. X. Deng and S. K. Zhong, Effect of Interlayer Anions on the Electrochemical Performance of Al-Substituted α-Type Nickel Hydroxide Electrodes, *Int. J. Hydrogen Energy*, 2010, **35**, 2539–2545.
27 W.-K. Hu and D. Noreus, Alpha Nickel Hydroxides as Lightweight Nickel Electrode Materials for Alkaline Rechargeable Cells, *Chem. Mater.*, 2003, **15**, 974–978.
28 L. Bing, Y. Huatang, Z. Yunshi, Z. Zuoxiang and S. Deying, Cyclic Voltammetric Studies of Stabilized α-Nickel Hydroxide Electrode, *J. Power Sources*, 1999, **79**, 277–280.
29 M. G. Ortiz and E. B. Castro, and S. G. y Real, The Cobalt Content Effect on the Electrochemical Behavior of Nickel Hydroxide Electrodes, *Int. J. Hydrogen Energy*, 2012, **37**, 10365–10370.
30 R. D. Armstrong, G. W. D. Briggs and E. A. Charles, Some Effects of the Addition of Cobalt to the Nickel Hydroxide Electrode, *J. Appl. Electrochem.*, 1988, **18**, 215–219.
31 D. A. Corrigan and R. M. Bendert, Effect of Coprecipitated Metal Ions on the Electrochemistry of Nickel Hydroxide Thin Films: Cyclic Voltammetry in 1 M KOH, *J. Electrochem. Soc.*, 1989, **136**, 723–728.
32 J. Bao, Y. Zhu, Z. Zhang, Q. Xu, W. Zhao, J. Chen, W. Zhang and Q. Han, Structure and Electrochemical Properties of Nanometer Cu Substituted α-Nickel Hydroxide, *Mater. Res. Bull.*, 2013, **48**, 422–428.
33 K. Ho Kim, M. Mikami, Y. Abe, M. Kawamura and T. Kiba, Structural and Electrochemical Properties of Nanolayer-Stacking Structured Copper-Doped Nickel Hydroxide, *Int. J. Electrochem. Sci.*, 2018, **13**, 7655–7662.
34 D. Zide, C. Felix, T. Oosthuysen and B. J. Bladergroen, The Influence of Copper and Carbon Black on Electrochemical Behavior of Nickel Positive Electrode, *J. Appl. Electrochem.*, 2020, **878**, 114539.
35 R. S. Jayashree and P. Vishnu Kamath, Layered Double Hydroxides of Ni with Cr and Mn as Candidate Electrode Materials for Alkaline Secondary Cells, *J. Power Sources*, 2002, **107**, 120–124.
36 M. Morishita, S. Ochiai, T. Kakeya, T. Ozaki, Y. Kawabe, M. Watada, S. Tanase and T. Sakai, Structural Analysis by Synchrotron XRD and XAFS for Manganese-Substituted α- and β-Type Nickel Hydroxide Electrode, *J. Electrochem. Soc.*, 2008, **155**, A936–A944.
37 X. L. Guo, X. Y. Liu, X. D. Hao, S. J. Zhu, F. Dong, Z. Q. Wen and Y. X. Zhang, Nickel-Manganese Layered Double Hydroxide Nanosheets Supported on Nickel Foam for High-Performance Supercapacitor Electrode Materials, *Electrochim. Acta*, 2016, **194**, 179–186.
38 C. C. Miao, Y. J. Zhu, L. G. Huang and T. Q. Zhao, Synthesis, Characterization, and Electrochemical Performances of Alpha Nickel Hydroxide by Coprecipitating Sn^{2+}, *Ionics*, 2015, **21**, 2295–2302.
39 C. Tessier, L. Guerlou-Demourgues, C. Faure, A. Demourgues and C. Delmas, Structural Study of Zinc-Substituted Nickel Hydroxides, *J. Mater. Chem.*, 2000, **10**, 1185–1193.

40 C. Tessier, C. Faure, L. Guerlou-Demourgues, C. Denage, G. Nabias and C. Delmas, Electrochemical Study of Zinc-Substituted Nickel Hydroxide, *J. Electrochem. Soc.*, 2002, **149**, A1136–A1145.

41 M. Dixit, R. S. Jayashree, P. Vishnu Kamath, A. K. Shukla, V. Ganesh Kumar and N. Munichandraiah, Electrochemically Impregnated Aluminum-Stabilized α-Nickel Hydroxide Electrode, *Electrochem. Solid-State Lett.*, 1999, **2**, 170–171.

42 C. Wang, X. Zhang, Z. Xu, X. Sun and Y. Ma, Ethylene Glycol Intercalated Cobalt/Nickel Layered Double Hydroxide Nanosheet Assemblies with Ultrahigh Specific Capacitance: Structural Design and Green Synthesis for Advanced Electrochemical Storage, *ACS Appl. Mater. Interfaces*, 2015, **7**, 19601–19610.

43 H. Huang, Y. Guo and Y. Cheng, Ultrastable α Phase Nickel Hydroxide as Energy Storage Materials for Alkaline Secondary Batteries, *Appl. Surf. Sci.*, 2018, **435**, 635–640.

44 K. H. Young, L. Wang, S. Yan, X. Liao, T. Meng, H. Shen and W. Mays, Fabrications of High-Capacity α-$Ni(OH)_2$, *Batteries*, 2017, **3**, 1–21.

45 D. S. Hall, D. J. Lockwood, C. Bock and B. R. MacDougall, Nickel Hydroxides and Related Materials: A Review of Their Structures, Synthesis and Properties, *Proc. R. Soc. A*, 2015, **471**, 20140792.

46 I. Bilecka and M. Niederberger, Microwave Chemistry for Inorganic Nanomaterials Synthesis, *Nanoscale*, 2010, **2**, 1358–1374.

47 F. Godínez-Salomón, L. Albiter, S. M. Alia, B. S. Pivovar, L. E. Camacho-Forero, P. B. Balbuena, R. Mendoza-Cruz, M. J. Arellano-Jimenez and C. P. Rhodes, Self-Supported Hydrous Iridium–Nickel Oxide Two-Dimensional Nanoframes for High Activity Oxygen Evolution Electrocatalysts, *ACS Catal.*, 2018, **8**, 10498–10520.

48 F. Godinez-Salomon, R. Mendoza-Cruz, M. J. Arellano-Jimenez, M. Jose-Yacaman and C. P. Rhodes, Metallic Two-Dimensional Nanoframes: Unsupported Hierarchical Nickel-Platinum Alloy Nanoarchitectures with Enhanced Electrochemical Oxygen Reduction Activity and Stability, *ACS Appl. Mater. Interfaces*, 2017, **9**, 18660–18674.

49 L. Xu, Y. Ding, C. Chen, L. Zhao, C. Rimkus, R. Joesten and S. L. Suib, 3D Flowerlike α-Nickel Hydroxide with Enhanced Electrochemical Activity Synthesized by Microwave-Assisted Hydrothermal Method, *Chem. Mater.*, 2008, **20**, 308–316.

50 M. Casas-Cabanas, J. Rodríguez-Carvajal, J. Canales-Vázquez and M. R. Palacín, New Insights on the Microstructural Characterisation of Nickel Hydroxides and Correlation with Electrochemical Properties, *J. Mater. Chem.*, 2006, **16**, 2925–2939.

51 C. Lamiel, V. H. Nguyen, D. R. Kumar and J.-J. Shim, Microwave-Assisted Binder-Free Synthesis of 3D Ni-Co-Mn Oxide Nanoflakes@Ni Foam Electrode for Supercapacitor Applications, *Chem. Eng. J.*, 2017, **316**, 1091–1102.

52 J. Li, M. Wei, W. Chu and N. Wang, High-Stable α-Phase NiCo Double Hydroxide Microspheres via Microwave Synthesis for Supercapacitor Electrode Materials, *Chem. Eng. J.*, 2017, **316**, 277–287.

53 Y. Tao, Z. Haiyan, L. Ruiyi, L. Zaijun, L. Junkang, W. Guangli and G. Zhiquo, Microwave Synthesis of Nickel/Cobalt Double Hydroxide Ultrathin Flowerclusters with Three-Dimensional Structures for High-Performance Supercapacitors, *Electrochim. Acta*, 2013, **111**, 71–79.

54 P. Benito, F. M. Labajos and V. Rives, Microwave-Treated Layered Double Hydroxides Containing Ni and Al: The Effect of Added Zn, *J. Solid State Chem.*, 2006, **179**, 3784–3797.

55 X. Ma, J. Liu, C. Liang, X. Gong and R. Che, A Facile Phase Transformation Method for the Preparation of 3D Flower-Like β-$Ni(OH)_2$/GO/CNTs Composite with Excellent Supercapacitor Performance, *J. Mater. Chem. A*, 2014, **2**, 12692–12696.

56 T. Malis, S. C. Cheng and R. F. Egerton, EELS Log-Ratio Technique for Specimen-Thickness Measurement in the TEM, *J. Electron Microsc. Tech.*, 1988, **8**, 193–200.

57 A. L. Brisse, P. Stevens, G. Toussaint, O. Crosnier and T. Brousse, $Ni(OH)_2$ and NiO Based Composites: Battery Type Electrode Materials for Hybrid Supercapacitor Devices, *Materials*, 2018, **11**, 1–15.

58 P. Bonnick and J. R. Dahn, A Simple Coin Cell Design for Testing Rechargeable Zinc-Air or Alkaline Battery Systems, *J. Electrochem. Soc.*, 2012, **159**, A981–A989.

59 M. Gong, Y. Li, H. Zhang, B. Zhang, W. Zhou, J. Feng, H. Wang, Y. Liang, Z. Fan, J. Liu and H. Dai, Ultrafast High-Capacity NiZn Battery with NiAlCo-Layered Double Hydroxide, *Energy Environ. Sci.*, 2014, **7**, 2025–2032.

60 Y. Zhang, Q. Shao, S. Long and X. Huang, Cobalt-Molybdenum Nanosheet Arrays as Highly Efficient and Stable Earth-abundant Electrocatalysts for Overall Water Splitting, *Nano Energy*, 2018, **45**, 448–455.

61 A. J. Smith, J. C. Burns and J. R. Dahn, High-Precision Differential Capacity Analysis of $LiMn_2O_4$/graphite Cells, *Electrochem. Solid-State Lett.*, 2011, **14**, A39–A41.

62 E. A. Cochran, K. N. Woods, D. W. Johnson, C. J. Page and S. W. Boettcher, Unique Chemistries of Metal-Nitrate Precursors to Form Metal-Oxide Thin Films from Solution: Materials for Electronic and Energy Applications, *J. Mater. Chem. A*, 2019, **7**, 24124–24149.

63 W. Yang, Z. Gao, J. Wang, J. Ma, M. Zhang and L. Liu, Solvothermal One-Step Synthesis of Ni-Al Layered Double Hydroxide/Carbon Nanotube/Reduced Graphene Oxide Sheet Ternary Nanocomposite with Ultrahigh Capacitance for Supercapacitors, *ACS Appl. Mater. Interfaces*, 2013, **5**, 5443–5454.

64 D. R. Rolison, Catalytic Nanoarchitectures—the Importance of Nothing and the Unimportance of Periodicity, *Science*, 2003, **299**, 1698–1701.

65 J. H. Choy, Y. M. Kwon, K. S. Han, S. W. Song and S. H. Chang, Intra- and Inter-Layer Structures of Layered Hydroxy Double salts, $Ni_{1-x}Zn_{2x}(OH)_2(CH_3CO_2)_{2x}{\cdot}nH_2O$, *Mater. Lett.*, 1998, **34**, 356–363.

66 Z. J. Zhang, Y. J. Zhu, J. Bao, X. R. Lin and H. Z. Zheng, Electrochemical Performance of Multi-Element Doped α-Nickel Hydroxide Prepared by Supersonic Co-Precipitation Method, *J. Alloys Compd.*, 2011, **509**, 7034–7037.

67 H. Li, J. Ma, D. G. Evans, T. Zhou, F. Li and X. Duan, Molecular Dynamics Modeling of the Structures and Binding Energies of α-Nickel Hydroxides and Nickel-Aluminum Layered Double Hydroxides Containing Various Interlayer Guest Anions, *Chem. Mater.*, 2006, **18**, 4405–4414.

68 M. Dixit, V. P. Kamath and J. Gopalakrishnan, Zinc-Substituted α-Nickel Hydroxide as an Electrode Material for Alkaline Secondary Cells, *J. Electrochem. Soc.*, 1999, **146**, 79–82.

69 D. Kundu, B. D. Adams, V. Duffort, S. H. Vajargah and L. F. Nazar, A High-Capacity and Long-Life Aqueous Rechargeable Zinc Battery Using a Metal Oxide Intercalation Cathode, *Nat. Energy*, 2016, **1**, 16111–16121.

70 D. Chen, X. Xiong, B. Zhao, M. A. Mahmoud, M. A. El-Sayed and M. Liu, Probing Structural Evolution and Charge Storage Mechanism of NiO_2H_x Electrode Materials using In Operando Resonance Raman Spectroscopy, *Adv. Sci.*, 2016, **3**, 1500433.

71 D. S. Hall, D. J. Lockwood, S. Poirier, C. Bock and B. R. MacDougall, Raman and Infrared Spectroscopy of Alpha and Beta Phases of Thin Nickel Hydroxide Films Electrochemically Formed on Nickel, *J. Phys. Chem. A*, 2012, **116**, 6771–6784.

72 D. K. Breitingera, J. Mohra, D. Colognesib, S. F. Parkerb, H. Schukowc and R. G. Schwabc, Vibrational Spectra of Augelites $Al_2(OH)_3(XO_4)$ (X = P, As, V), *J. Mol. Struct.*, 2001, **563-564**, 377–382.

73 S. R. Shieh and T. S. Duffy, Raman Spectroscopy of $Co(OH)_2$ at High Pressures: Implications for Amorphization and Hydrogen Repulsion, *Phys. Rev. B: Condens. Matter Mater. Phys.*, 2002, **66**, 134301.

74 C. Juliena, M. Massotb, R. Baddour-Hadjeanc, S. Frangerd, S. Bachd and J. P. Pereira-Ramosd, Raman Spectra of Birnessite Manganese Dioxides, *Solid State Ionics*, 2003, **159**, 345–356.

75 S. U. Awan, S. K. Hasanain, J. Rashid, S. Hussain, S. A. Shah, M. Z. Hussain, M. Rafique, M. Aftab and R. Khan, Structural, Optical, Electronic and Magnetic Properties of Multiphase $ZnO/Zn(OH)_2/ZnO_2$ Nanocomposites and Hexagonal Prism Shaped ZnO Nanoparticles Synthesized by Pulse Laser Ablation in Heptanes, *Mater. Chem. Phys.*, 2018, **211**, 510–521.

76 R. Cuscó, E. Alarcón-Lladó, J. Ibáñez, L. Artús, J. Jiménez, B. Wang and M. J. Callahan, Temperature Dependence of Raman Scattering in ZnO, *Phys. Rev. B: Condens. Matter Mater. Phys.*, 2007, **75**, 165202.

77 W. Sawodny, K. Niedenzu and J. W. Dawson, The Vibrational Spectrum of Ethylene Glycol, *Spectrochim. Acta, Part A*, 1967, **23**, 799–806.

78 J. Wu and H. Zheng, Quantitative Measurement of the Concentration of Sodium Carbonate in the System of Na_2CO_3–H_2O by Raman spectroscopy, *Chem. Geol.*, 2010, **273**, 267–271.

79 Y. Ma, W. Yan, Q. Sun and X. Liu, Raman and Infrared Spectroscopic Quantification of the Carbonate Concentration in K_2CO_3 Aqueous Solutions with Water as an Internal Standard, *Geosci. Front.*, 2021, **12**, 1018–1030.

80 B. Rousseau, R. Keuleers, H. O. Desseyn, H. J. Geise and C. Van, Alsenoy, Solids Modeled by Ab-Initio Crystal Field Methods. Effects of Intermolecular Interactions on the Vibrational Spectrum of Urea, *Chem. Phys. Lett.*, 1999, **302**, 55–59.

81 M. S. Lowenthal, R. K. Khanna and M. H. Moore, Infrared Spectrum of Solid Isocyanic Acid (HNCO): Vibrational Assignments and Integrated Band Intensities, *Spectrochim. Acta, Part A*, 2002, **58**, 73–78.

82 M. H. Brooker and N. Wen, Raman Studies of Cyanate: Fermi Resonance, Hydration and Hydrolysis to Urea, *Can. J. Chem.*, 1993, **71**, 1764–1773.

83 F. F. Cleveland, Raman Spectrum of an Aqueous Solution of Potassium Cyanate, *J. Am. Chem. Soc.*, 1941, **63**, 622–623.

84 A. J. Smith and J. R. Dahn, Delta Differential Capacity Analysis, *J. Electrochem. Soc.*, 2012, **159**, A290–A293.

85 M. Vidotti, R. P. Salvador, E. A. Ponzio and S. I. Córdoba de Torresi, Mixed Ni/Co Hydroxide Nanoparticles Synthesized by Sonochemical Method, *J. Nanosci. Nanotechnol.*, 2007, **7**, 3221–3226.

86 J. Wu, W.-W. Liu, Y.-X. Wu, T.-C. Wei, D. Geng, J. Mei, H. Liu, W.-M. Lau and L.-M. Liu, Three-Dimensional Hierarchical Interwoven Nitrogen-Doped Carbon Nanotubes/Co_xNi_{1-x}-Layered Double Hydroxides Ultrathin Nanosheets for High-Performance Supercapacitors, *Electrochim. Acta*, 2016, **203**, 21–29.

87 C. Miao, Y. Zhu, L. Huang and T. Zhao, The Relationship Between Structural Stability and Electrochemical Performance of Multi-element Doped Alpha Nickel Hydroxide, *J. Power Sources*, 2015, **274**, 186–193.

88 M. Dixita, P. Vishnu Kamatha, V. Ganesh Kumarb, N. Munichandraiahc and A. K. Shuklab, An Electrochemically Impregnated Sintered-Nickel Electrode, *J. Power Sources*, 1996, **63**, 167–171.

89 C. Liu and Y. Li, Synthesis and Characterization of Amorphous α-Nickel Hydroxide, *J. Alloys Compd.*, 2009, **478**, 415–418.

90 M. Hu, Z. Yang, L. Lei and Y. Sun, Structural Transformation and its Effects on the Electrochemical Performances of a Layered Double Hydroxide, *J. Power Sources*, 2011, **196**, 1569–1577.

91 M. Morishita, T. Kakeya, S. Ochiai, T. Ozaki, Y. Kawabe, M. Watada and T. Sakai, Structural Analysis by Synchrotron X-ray Diffraction, X-ray Absorption Fine Structure and Transmission Electron Microscopy for Aluminum-Substituted α-Type Nickel Hydroxide Electrode, *J. Power Sources*, 2009, **193**, 871–877.

92 O. Diaz-Morales, I. Ledezma-Yanez, M. T. M. Koper and F. Calle-Vallejo, Guidelines for the Rational Design of Ni-Based Double Hydroxide Electrocatalysts for the Oxygen Evolution Reaction, *ACS Catal.*, 2015, **5**, 5380–5387.

93 A. Hartig-Weiss, M. F. Tovini, H. A. Gasteiger and H. A. El-Sayed, OER Catalyst Durability Tests Using the Rotating Disk Electrode Technique: The Reason Why This Leads to Erroneous Conclusions, *ACS Appl. Energy Mater.*, 2020, **3**, 10323–10327.

94 J. W. Lee, J. M. Ko and J.-D. Kim, Hierarchical Microspheres Based on α-Ni(OH)$_2$ Nanosheets Intercalated with Different Anions: Synthesis, Anion Exchange, and Effect of Intercalated Anions on Electrochemical Capacitance, *J. Phys. Chem. C*, 2011, **115**, 19445–19454.

95 E. Shangguan, J. Li, D. Guo, L. Guo, M. Nie, Z. Chang, X.-Z. Yuan and H. Wang, A Comparative Study of Structural and Electrochemical Properties of High-Density Aluminum Substituted α-Nickel Hydroxide Containing Different Interlayer Anions, *J. Power Sources*, 2015, **282**, 158–168.